GDCh

Research Articles

Angewandte
Chemie
International Edition
www.angewandte.org

VIP **Hydrogen Production** *Very Important Paper*

Heteroatom-Doped Ag$_{25}$ Nanoclusters Encapsulated in Metal–Organic Frameworks for Photocatalytic Hydrogen Production

He Wang, Xiyuan Zhang, Wei Zhang, Meng Zhou,* and Hai-Long Jiang*

Abstract: Atomically precise metal nanoclusters (NCs) with unique optical properties and abundant catalytic sites are promising in photocatalysis. However, their light-induced instability and the difficulty of utilizing the photogenerated carriers for photocatalysis pose significant challenges. Here, MAg_{24} (M = Ag, Pd, Pt, and Au) NCs doped with diverse single heteroatoms have been encapsulated in a metal–organic framework (MOF), UiO-66-NH$_2$, affording MAg_{24}@UiO-66-NH$_2$. Strikingly, compared with Ag_{25}@UiO-66-NH$_2$, the MAg_{24}@UiO-66-NH$_2$ doped with heteroatom exhibits much enhanced activity in photocatalytic hydrogen production, among which $AuAg_{24}$@UiO-66-NH$_2$ presents the best activity up to 3.6 mmol g^{-1} h^{-1}, far superior to all other counterparts. Moreover, they display excellent photocatalytic recyclability and stability. X-ray photoelectron spectroscopy and ultrafast transient absorption spectroscopy demonstrate that MAg_{24} NCs encapsulated into the MOF create a favorable charge transfer pathway, similar to a Z-scheme heterojunction, when exposed to visible light. This promotes charge separation, along with optimized Ag electronic state, which are responsible for the superior activity in photocatalytic hydrogen production.
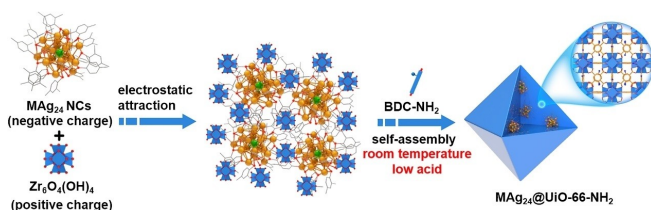
Introduction

The conversion of solar energy into chemical energy is widely recognized as a sustainable and promising strategy to mitigate environmental issues and the energy crisis.[1] In particular, solar-powered photocatalytic water splitting technology has attracted great attention due to its capability to produce hydrogen from water based on readily

[*] H. Wang, X. Zhang, Dr. W. Zhang, Prof. Dr. M. Zhou, Prof. Dr. H.-L. Jiang
Hefei National Research Center for Physical Sciences at the Microscale, University of Science and Technology of China, Hefei, Anhui 230026, P. R. China
E-mail: mzhou88@ustc.edu.cn
        jianglab@ustc.edu.cn
Homepage: http://mof.ustc.edu.cn/

H. Wang, X. Zhang, Prof. Dr. H.-L. Jiang
Department of Chemistry,
University of Science and Technology of China,
Hefei, Anhui 230026, P. R. China

available solar energy.[2] In recent years, metal nanoclusters (NCs) with atomic-level structural precision have shown potential applications in solar energy harvesting and conversion because of their unique atomic stacking mode, quantum confinement effect, and abundant catalytic active sites.[3] However, metal NCs are structurally unstable during photocatalysis and are very susceptible to self-oxidation resulting in migratory aggregation. Moreover, the difficulty of utilizing the photogenerated carriers limits their applications in photocatalysis.[4] In this context, the encapsulation of metal NCs into crystalline porous materials would provide an opportunity to stabilize metal NCs and construct efficient photocatalytic systems.[5] On the one hand, the confinement effect of the crystalline porous materials would effectively inhibit the migration and aggregation of metal NCs.[6] On the other hand, the metal NCs can be considered as narrow band gap semiconductors due to the discrete molecular-like energy band structure that is different from common metal nanoparticles; heterojunction photocatalytic systems can be formed by constructing composites involving semiconductor-like crystal porous materials and metal NCs to extend the lifetime of photoexcited charge carriers for enhanced photocatalysis.[7]

As a class of porous crystalline materials, metal–organic frameworks (MOFs), featuring well-defined and tailorable structures, high porosity, and specific surface area,[8] have been composited with a variety of functional materials.[9] Particularly, given MOFs have been demonstrated to be very good hosts and supports to stabilize metal nanoparticles,[10] they would be also suitable for encapsulating metal NCs from aggregation.[11] Moreover, MOFs are highly tunable in light harvesting from UV to near-infrared regions, which might be simultaneously photoexcited with metal NCs to constitute a heterojunction photocatalytic system for promoted charge separation. Despite a few reports on the stabilization of metal NCs with MOFs for photocatalysis,[5a,7b] the formation of heterojunction or related mechanisms for enhanced photocatalysis has not yet been observed in these composites.

In this work, four MAg_{24} (M = Ag, Pd, Pt, Au) NCs have been encapsulated into a representative visible-light-responsive MOF, UiO-66-NH$_2$, via electrostatic interactions to afford MAg_{24}@UiO-66-NH$_2$, in which the only difference is the single-atom metal at the cluster core (Scheme 1). Remarkably, Ag_{25}@UiO-66-NH$_2$ presents outstanding activity, with hydrogen production rate of ~5.6 times higher than that of Ag_{NPs}@UiO-66-NH$_2$ and ~6.4 times higher than that of Ag_{25} supported on UiO-66-NH$_2$, and maintains excellent stability in the photocatalytic

Scheme 1. Illustration showing the synthetic route to MAg$_{24}$@UiO-66-NH$_2$ by encapsulating MAg$_{24}$ clusters into UiO-66-NH$_2$ via electrostatic attraction and self-assembly at room temperature under low-acidity conditions.

hydrogen production. When doping heteroatom metal in the center of MAg$_{24}$ clusters, the activity is further improved in the order of AuAg$_{24}$ > PtAg$_{24}$ > PdAg$_{24}$ > Ag$_{25}$. The AuAg$_{24}$@UiO-66-NH$_2$ exhibits the highest hydrogen production rate of 3.6 mmol g^{-1} h^{-1}, which is ~4.8 times higher than that of Ag$_{25}$@UiO-66-NH$_2$. Femtosecond transient absorption spectroscopy demonstrates that the charge carrier lifetime is significantly enhanced after these metal NCs being encapsulated in the MOF, and the sequence is consistent with the order of photocatalytic hydrogen production rate. In situ X-ray photoelectron spectroscopy (XPS) indicates the formation of a Z-scheme heterojunction system, which is responsible for efficient charge separation. To the best of our knowledge, this is the first report on the formation of a Z-scheme photocatalytic system with metal NCs-MOF composites for enhanced photocatalysis.

Results and Discussion

Four similar structured MAg$_{24}$ (M = Ag, Pd, Pt, and Au) capped by 2,4-dimethylbenzenethiolate are selected as representative metal NCs, as they have excellent photosensitivity and stabilized superatomic properties.[12] The single Ag atom in the center of Ag$_{25}$ NCs is readily replaced by other metal atoms, such as Pd, Pt, or Au, to give MAg$_{24}$ NCs. These metal NCs with high purity were synthesized by the kinetically controlled method and confirmed by UV/Vis absorption spectroscopy (Figure S1).[12] To avoid the structural destruction of MAg$_{24}$ NCs in the common solvothermal conditions for MOF synthesis, the self-assembly strategy for the Zr$_6$-oxo clusters and 2-aminoterephthalic acid (NH$_2$-BDC) at room temperature was adopted.[5c] The MAg$_{24}$ NCs are negatively charged, whereas the pre-synthesized Zr$_6$-oxo clusters and UiO-66-NH$_2$ are positively charged as measured by the zeta potential (Table S1). Given their reversed charges, MAg$_{24}$ can be electrostatically attracted onto Zr$_6$-oxo clusters, followed by further MOF growth to afford MAg$_{24}$@UiO-66-NH$_2$. Or else, the direct supporting MAg$_{24}$ onto the outer surface of UiO-66-NH$_2$ by electrostatic interaction,[13] producing MAg$_{24}$/UiO-66-NH$_2$.

Powder X-ray diffraction (XRD) patterns show that the introduction of MAg$_{24}$ does not affect the MOF crystal-

linity in MAg$_{24}$@UiO-66-NH$_2$ composites (Figure S2). UV/Vis diffuse reflectance spectra of the composites display the characteristic absorption peaks of MAg$_{24}$ NCs, suggesting that the structure of MAg$_{24}$ NCs is well maintained (Figure S3). Nitrogen sorption indicates that all composites are highly porous and the BET surface areas of MAg$_{24}$@UiO-66-NH$_2$ (746–771 m^2/g) are slightly lower than Ag$_{25}$/UiO-66-NH$_2$ (880 m^2/g) and UiO-66-NH$_2$ (923 m^2/g) (Figure S4), which might be due to the occupation of the MOF pore space by MAg$_{24}$ NCs in MAg$_{24}$@UiO-66-NH$_2$.

In addition, no apparent aggregation and size change for metal NCs in Ag$_{25}$@UiO-66-NH$_2$ and Ag$_{25}$/UiO-66-NH$_2$ can be observed from the high-angle annular dark-field scanning transmission electron microscopy (HAADF-STEM) images compared to the parent Ag$_{25}$ NCs (Figure 1a, b, S5). By directly comparing the HAADF-STEM and secondary electron STEM (SE-STEM) images at the same location, it is evident that Ag$_{25}$ NCs are incorporated into and supported on the external surface of the MOF
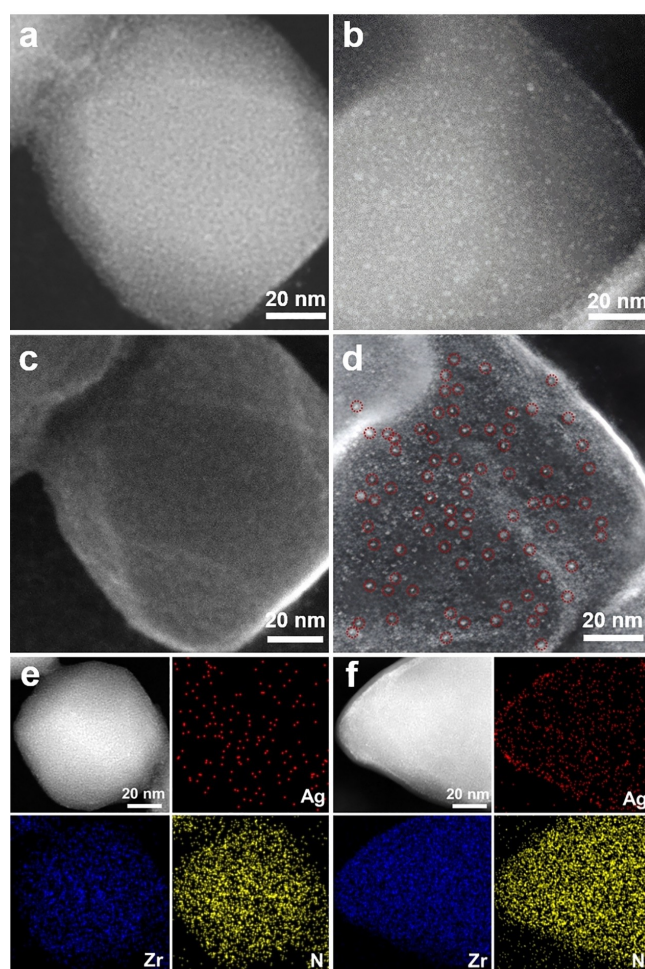

Figure 1. (a, b) HAADF-STEM images and (c, d) SE-STEM images of (a, c) Ag$_{25}$@UiO-66-NH$_2$ and (b, d) Ag$_{25}$/UiO-66-NH$_2$ (inset of d: the readily distinguishable Ag$_{25}$ NCs on the MOF particle are highlighted with red circles). HAADF-STEM images and the corresponding EDS mapping of Ag, Zr, and N elements for (e) Ag$_{25}$@UiO-66-NH$_2$ and (f) Ag$_{25}$/UiO-66-NH$_2$.

particle in Ag_{25}@UiO-66-NH_2 and Ag_{25}/UiO-66-NH_2, respectively (Figure 1c, d). The energy dispersive X-ray spectroscopy (EDS) mapping analysis indicates that the Ag species in Ag_{25}@UiO-66-NH_2 is uniformly dispersed throughout the MOF particle (Figure 1e), while the Ag species in Ag_{25}/UiO-66-NH_2 is mainly distributed at the MOF particulate edges (Figure 1f), which is in good agreement with the above SE-STEM results. The other $PdAg_{24}$, $PtAg_{24}$, and $AuAg_{24}$ NCs are similarly dispersed throughout the MOF particle as supported by HAADF-STEM and EDS mapping observation (Figures S6–S8).

As a control, Ag_{NPs}@UiO-66-NH_2, encapsulating Ag nanoparticles inside UiO-66-NH_2, was also synthesized. Powder XRD results and N_2 sorption results indicate the synthetic process barely influences the MOF structure (Figure S9). The HADDF-STEM and EDS mapping results also indicate that Ag nanoparticles are also well dispersed inside the MOF (Figure S10). Scanning electron microscope (SEM) images indicate that the particle size and morphology are similar to each other in all these composites (Figure S11). The Ag loading amount is controlled to be comparable of ~1.5 wt% and the doped Pd/Pt/Au content is as low as ~0.1 wt% in Ag_{NPs}@UiO-66-NH_2, Ag_{25}/UiO-66-NH_2 and MAg_{24}@UiO-66-NH_2 according to inductively coupled plasma atomic emission spectroscopy (ICP-AES) results (Table S2).

Motivated by the results above, photocatalytic H_2 production experiments have been carried out under visible light irradiation using TEA as the electron donor. The photocatalytic H_2 production activity over UiO-66-NH_2 is as low as 10.2 $\mu mol\,g^{-1}\,h^{-1}$, and Ag_{25} NCs shows almost negligible activity (Figure 2a). Upon integrating Ag_{25} NCs with the MOF, the activity is significantly increased and the location of Ag_{25} relative to the MOF particle significantly

affects the activity. Specifically, the hydrogen production rate over Ag_{25}@UiO-66-NH_2 is up to 739.4 $\mu mol\,g^{-1}\,h^{-1}$, ~6.4 times higher than Ag_{25}/UiO-66-NH_2 (115.3 $\mu mol\,g^{-1}\,h^{-1}$) (Figure 2a). In the cycling experiments, the hydrogen production rate of Ag_{25}@UiO-66-NH_2 can be maintained during the three photocatalytic cycles of 6 h; in contrast, the activity of Ag_{25}/UiO-66-NH_2 displays a noticeable decrease, which may be due to the unexpected leaching and/or aggregation of Ag_{25} NCs (Figure 2b, Table S2). HADDF-STEM images reveal that the size and dispersion of Ag_{25} NCs in Ag_{25}@UiO-66-NH_2 remain unchanged after three cycles of reaction thanks to the confinement and protection by the MOF structure while significant agglomeration occurs in Ag_{25}/UiO-66-NH_2 (Figure S12), accounting for their distinct cycling performance. Moreover, the activity of Ag_{25}@UiO-66-NH_2 is ~5.6 times higher than that of Ag_{NPs}@UiO-66-NH_2 (131.8 $\mu mol\,g^{-1}\,h^{-1}$), highlighting the photocatalytic advantages of metal NCs with better dispersion and smaller sizes. These results suggest that MOF encapsulation not only promotes photocatalytic hydrogen production rate but also improves the stability of metal NCs.

Given that the introduction of heteroatom dopants in metal NCs is able to modulate its energy band structure and contributes to the redistribution of the surface charge, thereby significantly affecting the physicochemical properties,[14] MAg_{24} NCs doped with central singe-atom Pd, Pt, or Au are investigated for photocatalytic hydrogen production. As expected, despite the only difference of central metal atom, MAg_{24}@UiO-66-NH_2 gives far superior activity to the parent Ag_{25}@UiO-66-NH_2, with activity in the trend of $AuAg_{24}$@UiO-66-NH_2 > $PtAg_{24}$@UiO-66-NH_2 > $PdAg_{24}$@UiO-66-NH_2 > Ag_{25}@UiO-66-NH_2. Specifically, $AuAg_{24}$@UiO-66-NH_2 exhibits the highest hydrogen production rate of 3576.3 $\mu mol\,g^{-1}\,h^{-1}$, which is ~4.8 times higher than that of Ag_{25}@UiO-66-NH_2 and also much higher than that of $PdAg_{24}$@UiO-66-NH_2 and $PtAg_{24}$@UiO-66-NH_2 (Figure 2c), as well as many other corresponding counterparts (Table S3). The evaluated apparent quantum efficiency (AQE) of $AuAg_{24}$@UiO-66-NH_2 under light irradiation at 380 nm is ~0.53%, a value similar to other MOF-based catalysts for photocatalytic H_2 production (Table S4). For all MAg_{24}@UiO-66-NH_2 (M = Ag, Pd, Pt, and Au), the structure of MAg_{24} NCs and the MOF crystallinity can be maintained and there is no leaching of metal NCs after the photocatalytic reaction (Figures S13 and S14, Table S2). Moreover, $AuAg_{24}$@UiO-66-NH_2 possesses consistent H_2 production activity in the five consecutive runs (Figure 2d). After that, $AuAg_{24}$ NCs remain small sizes and uniformly dispersed inside the MOF (Figure S15), and the MOF integrity and crystallinity are well retained (Figure S16).

To understand the significant activity differences in MAg_{24}@UiO-66-NH_2 and the corresponding counterparts, relevant characterizations have been performed to elucidate the underlying mechanisms. Steady-state photoluminescence (PL) spectra under 380 nm excitation reveal a broadband center at ~450 nm for the MOF and all composites, while their intensities are significantly differ-
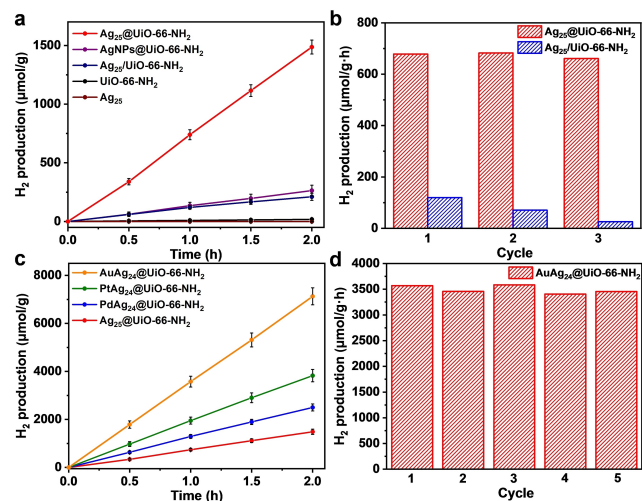

Figure 2. (a) Kinetic profiles of photocatalytic H_2 production over UiO-66-NH_2, Ag_{25}, Ag_{25}/UiO-66-NH_2, Ag_{25}@UiO-66-NH_2, and Ag_{NPs}@UiO-66-NH_2. (b) Cycling experiments of Ag_{25}@UiO-66-NH_2 and Ag_{25}/UiO-66-NH_2 in photocatalytic hydrogen production. (c) Kinetic profiles of photocatalytic H_2 production over MAg_{24}@UiO-66-NH_2. (d) Photocatalytic cycling performance of $AuAg_{24}$@UiO-66-NH_2.

ent. The decrease of the photoluminescence signal intensity in the composites reflects efficient transfer of electrons from the MOF to metal NCs; the highest electron transfer efficiency is found for $AuAg_{24}$@UiO-66-NH_2, followed by $PtAg_{24}$@UiO-66-NH_2, $PdAg_{24}$@UiO-66-NH_2, Ag_{25}@UiO-66-NH_2, Ag_{NPs}@UiO-66-NH_2, Ag_{25}@UiO-66-NH_2, and UiO-66-NH_2 (Figure S17). Moreover, the shorter PL lifetime reflects more efficient electron transfer. The fitting of the time-resolved PL spectra determines the PL lifetimes of 0.54 ns (UiO-66-NH_2), 0.39 ns (Ag_{25}/UiO-66-NH_2), 0.36 ns (Ag_{NPs}@UiO-66-NH_2), 0.33 ns (Ag_{25}@UiO-66-NH_2), 0.32 ns ($PdAg_{24}$@UiO-66-NH_2), 0.27 ns ($PtAg_{24}$@UiO-66-NH_2) and 0.18 ns ($AuAg_{24}$@UiO-66-NH_2) (Figure S18), indicating that MOF capsulation and heteroatom doping in NCs can improve electron transfer efficiency. To compare the electron–hole separation efficiency, the photocurrent tests suggest the strongest response of $AuAg_{24}$@UiO-66-NH_2 and the intensity of different composites follows the same trend as the degree of fluorescence decay (Figure S19), which suggests that MOF encapsulation and heteroatom doping in the center of metal NCs promote the separation of electron-hole pairs. This is also confirmed by electrochemical impedance spectroscopy (EIS), in which all the composites have smaller radii than the parent MOF and $AuAg_{24}$@UiO-66-NH_2 shows the smallest radius, indicating the lowest interfacial charge transfer resistance (Figure S20). The order of charge transfer and separation efficiency of all photocatalysts is in good agreement with the sequence of photocatalytic hydrogen production, reflecting the importance of charge transfer in the photocatalytic process of these composites.

The charge carrier dynamics of these photocatalysts in real time has been monitored by the femtosecond time-resolved transient absorption (fs-TA) spectroscopy (Figure 3a, S21). Before and after metal NCs are introduced into the MOF, the fs-TA spectra remain similar and they mainly exhibit the signal of UiO-66-NH_2 due to the low loading (~1.5 %) of metal NCs. To further demonstrate the influence of introducing metal NCs on the excited state dynamics of UiO-66-NH_2, the fs-TA spectra of these photocatalysts taken at 20 ps probe delay are normalized at 725 nm (Figure 3b). It can be seen that the intensity of the fs-TA peak near 630 nm decreases significantly after introducing metal NCs into the MOF, which reflects the efficient electron transfer from the MOF upon excitation.[15] The order of decreasing degree is $AuAg_{24}$@UiO-66-NH_2 > $PtAg_{24}$@UiO-66-NH_2 > $PdAg_{24}$@UiO-66-NH_2 > Ag_{25}@UiO-66-NH_2, in consistent with the order of photocatalytic activity, indicating that electron transfer is critical for promoting photocatalytic performance.

To further reveal the excited state kinetics of these photocatalysts, their fs-TA kinetics and fittings at 630 nm are compared. All TA kinetic taces can be fitted using a three-exponential decay function after deconvolution (fitting parameters in Table S5). The average relaxation lifetime is 168.7, 157.3, 212.4, and 264.2 ps for UiO-66-NH_2, Ag_{NPs}@UiO-66-NH_2, Ag_{25}/UiO-66-NH_2 and Ag_{25}@UiO-66-NH_2, respectively (Figure 3c). The results show a significant increase in the relaxation lifetime of Ag_{25}@UiO-66-

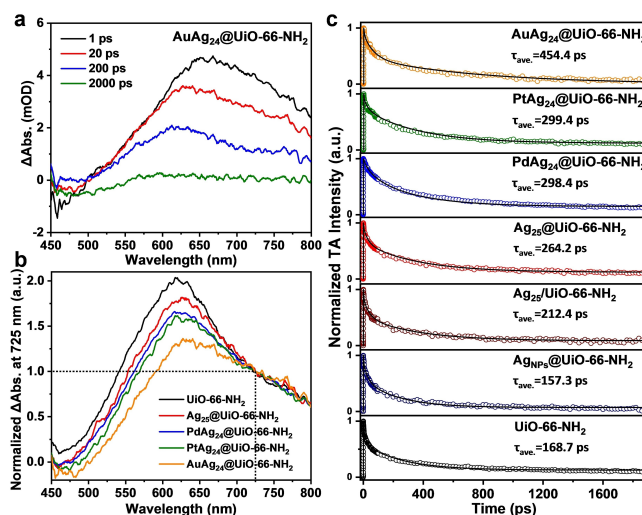*Figure 3.* (a) The fs-TA spectra (pump at 380 nm) taken at several representative time delays for $AuAg_{24}$@UiO-66-NH_2. (b) Normalized fs-TA spectra at 725 nm taken at 20 ps probe delay for UiO-66-NH_2 and MAg_{24}@UiO-66-NH_2 (pumps at 380 nm). (c) fs-TA kinetics probed near 630 nm and the corresponding multi-exponential fits of UiO-66-NH_2, Ag_{NPs}@UiO-66-NH_2, Ag_{25}/UiO-66-NH_2, Ag_{25}@UiO-66-NH_2 and MAg_{24}@UiO-66-NH_2 (M = Pd, Pt, and Au).

NH_2 compared to Ag_{NPs}@UiO-66-NH_2 and Ag_{25}/UiO-66-NH_2, which indicates that the MOF-encapsulated metal NCs are favorable for efficient separation of photogenerated electron-hole pairs. The average relaxation lifetime is also significantly different in MAg_{24}@UiO-66-NH_2 and the sequence is $AuAg_{24}$@UiO-66-NH_2 (454.4 ps) > $PtAg_{24}$@UiO-66-NH_2 (299.4 ps) > $PdAg_{24}$@UiO-66-NH_2 (298.4 ps) > Ag_{25}@UiO-66-NH_2 (264.2 ps) (Figure 3c). This demonstrates that suitable heteroatom-doped metal NCs can significantly inhibit the combination of photogenerated electrons and holes. Based on the above characterization results, it can be concluded that the encapsulation of metal NCs into MOFs as well as appropriate heteroatom doping significantly promotes charge migration and inhibits photogenerated electron and hole recombination, which is essential for improving the activity in the photocatalytic hydrogen production.

To disclose the photoinduced charge transfer pathways in the MAg_{24}@UiO-66-NH_2 system, the band structures of UiO-66-NH_2 and MAg_{24} NCs are evaluated first. The band gap of 2.98 eV for UiO-66-NH_2 is determined by the UV/Vis absorption spectrum and the lowest unoccupied molecular orbital (LUMO) level is estimated by Mott–Schottky measurements to be −0.59 V vs. NHE (Figure S22). Since metal NCs can be regarded as small band gap semiconductors,[7a] the energy band structure of MAg_{24} NCs is determined in the same way as for UiO-66-NH_2 (Figures S23 and S24). The energy diagram displays that all the LUMO positions of the MAg_{24} NCs are slightly lower than the LUMO level of UiO-66-NH_2, suggesting that they are thermodynamically capable of H_2O reduction (−0.40 V vs. NHE, pH 6.8) (Figure S25). Despite this, no H_2 production can be observed with individual metal NCs

under photocatalytic conditions (Figure S26), possibly due to their low HOMO (highest occupied molecular orbital) level, with which the holes cannot be consumed by TEA (Figure S25).[16] Surprisingly, the integration of them with UiO-66-NH$_2$ can give high H$_2$ production activity as discussed above (Figure 2), which might be attributed to the formation of heterojunction.[17]

In order to verify the possible heterojunction formation and examine the direction of charge transfer in MAg$_{24}$@UiO-66-NH$_2$, XPS and SI-XPS techniques are adopted, by which electron density change of various metal atoms in the excited state can be probed.[18] In the absence of light irradiation, the Zr 3d$_{5/2}$ XPS signal of MAg$_{24}$@UiO-66-NH$_2$ exhibits a shift to a higher binding energy than that of UiO-66-NH$_2$ (Figure S27), possibly due to the transfer of electrons from the MOF to the metal NCs, which would give rise to a downward energy band bending of the MOF.[19] Under light irradiation, the Zr 3d$_{5/2}$ binding energy of MAg$_{24}$@UiO-66-NH$_2$ manifests a positive shift (Figures 4a, S28a, S29a, and S30a), suggesting decreased electron density of the MOF. Meanwhile, the Ag 3d$_{5/2}$ binding energy of MAg$_{24}$@UiO-66-NH$_2$ has a negative shift (Figures 4b, S28b, S29b, and S30b), indicating increased electron density of the metal NCs. Upon light off, the binding energy of Ag 3d$_{5/2}$ and Zr 3d$_{5/2}$ in MAg$_{24}$@UiO-66-NH$_2$ return to their original position, supporting the reversibility of light-induced electron transfer in the composites. These binding energy changes provide direct evidence on the migration pathways of charge carriers, specifically, from the MOF to MAg$_{24}$, at the MAg$_{24}$@UiO-66-NH$_2$ interface under light irradiation, which unambiguously supports the formation of the direct Z-scheme mechanism (Figure 4c).[20]

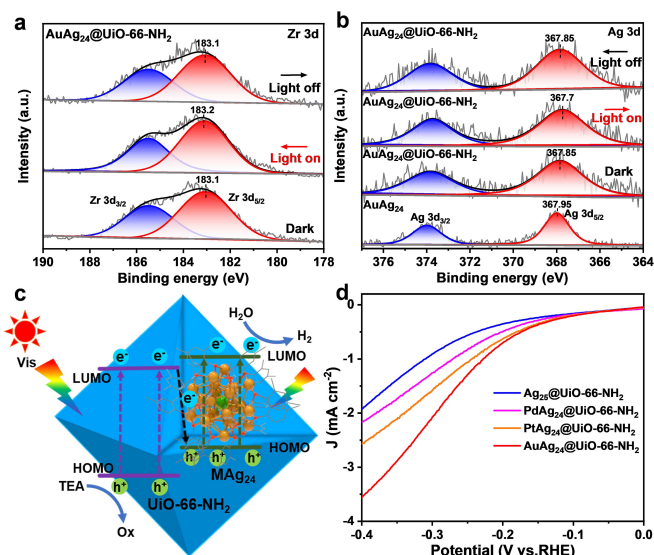In addition to the charge separation mechanism, the activity of MAg$_{24}$@UiO-66-NH$_2$ is also closely related to the electronic state of catalytic metal sites. Based on the above results, electrons excited to the LUMO of MAg$_{24}$ NCs would reduce the adsorbed protons to produce hydrogen. Therefore, the electron density of Ag sites on the MAg$_{24}$ surface is critical for the activity. The Ag electron density in MAg$_{24}$@UiO-66-NH$_2$ evaluated by XPS spectra follows the trend of Ag$_{25}$ < PdAg$_{24}$ < PtAg$_{24}$ < AuAg$_{24}$, suggesting that the central metal species is able to modulate the electron density of Ag on the surface (Figure S31). The intrinsic proton reduction capability of the surface Ag sites in the composites has been assessed by electrochemical hydrogen-evacuation reaction (HER) measurements. The hydrogen evolution overpotential showcases an order of AuAg$_{24}$@UiO-66-NH$_2$ < PtAg$_{24}$@UiO-66-NH$_2$ < PdAg$_{24}$@UiO-66-NH$_2$ < Ag$_{25}$@UiO-66-NH$_2$, suggesting that the surface reaction efficiency improves along with increased Ag electron density (Figure 4d).

Conclusion

In summary, for the first time, atomically precise MAg$_{24}$ (M = Ag, Pd, Pt, Au) NCs have been encapsulated into a MOF, namely UiO-66-NH$_2$, by electrostatic attraction and self-assembly to afford MAg$_{24}$@UiO-66-NH$_2$ composites for visible-light photocatalytic H$_2$ production. Strikingly, AuAg$_{24}$@UiO-66-NH$_2$ exhibits the best activity with H$_2$ production rate up to 3.6 mmol g^{-1} h^{-1}, far superior to the other counterparts, ~4.8, ~2.8 and ~1.8 times higher than that of Ag$_{25}$@UiO-66-NH$_2$, PdAg$_{24}$@UiO-66-NH$_2$, and PtAg$_{24}$@UiO-66-NH$_2$, respectively, highlighting the critical role of central heteroatom in the photocatalysis of metal NCs. Moreover, the H$_2$ production rate of Ag$_{25}$@UiO-66-NH$_2$ is ~6.4 and ~5.6 times higher than that of Ag$_{25}$/UiO-66-NH$_2$ and Ag$_{NPs}$@UiO-66-NH$_2$, respectively, which indicates that the encapsulation of small metal NCs into MOFs is favorable. Thanks to the MOF confinement, all these MOF-encapsulated metal NCs display excellent photocatalytic stability and recyclability. The XPS and transient absorption spectroscopy results demonstrate that MAg$_{24}$@UiO-66-NH$_2$ constitute a Z-scheme heterojunction system with suppressed charge recombination, where the photocatalytic H$_2$ production rate is closely associated with both charge transfer efficiency and the electronic state of surface Ag sites, accounting for their very high activity. This work unprecedentedly encapsulates heteroatom-doped metal NCs into MOFs, constituting a Z-scheme heterojunction system, which greatly improves photocatalytic hydrogen production activity and stability, and paves the way to the fabrication of structurally precise and customizable heterogeneous photocatalysts.

Figure 4. High-resolution SI-XPS spectra of (a) Zr 3d and (b) Ag 3d for AuAg$_{24}$@UiO-66-NH$_2$ in the dark and under in situ light irradiation. (c) Schematic illustration showing the formation of direct Z-scheme heterojunction and the electron migration at the MAg$_{24}$-MOF interface based on the energy levels. (d) Linear sweep voltammetry (LSV) curves of MAg$_{24}$@UiO-66-NH$_2$.

Acknowledgements

Conflict of Interest

The authors declare no conflict of interest.

Data Availability Statement

The data that support the findings of this study are available from the corresponding author upon reasonable request.

[1] a) J. Lv, J. Xie, A. G. A. Mohamed, X. Zhang, Y. Feng, L. Jiao, E. Zhou, D. Yuan, Y. Wang, *Nat. Chem. Rev.* **2023**, *7*, 91–105; b) Q. Wang, C. Pornrungroj, S. Linley, E. Reisner, *Nat. Energy* **2022**, *7*, 13–24; c) C. Feng, Z.-P. Wu, K.-W. Huang, J. Ye, H. Zhang, *Adv. Mater.* **2022**, *34*, 2200180.

[2] a) Z. Wang, C. Li, K. Domen, *Chem. Soc. Rev.* **2019**, *48*, 2109–2125; b) Y. Wang, H. Suzuki, J. Xie, O. Tomita, D. J. Martin, M. Higashi, D. Kong, R. Abe, J. Tang, *Chem. Rev.* **2018**, *118*, 5201–5241; c) S. Navalón, A. Dhakshinamoorthy, M. Álvaro, B. Ferrer, H. García, *Chem. Rev.* **2023**, *123*, 445–490.

[3] a) R. Jin, G. Li, S. Sharma, Y. Li, X. Du, *Chem. Rev.* **2021**, *121*, 567–648; b) X. Kang, Y. Li, M. Zhu, R. Jin, *Chem. Soc. Rev.* **2020**, *49*, 6443–6514; c) Y. Wang, X.-H. Liu, R. Wang, B. Cula, Z.-N. Chen, Q. Chen, N. Koch, N. Pinna, *J. Am. Chem. Soc.* **2021**, *143*, 9595–9600; d) M. Cao, R. Pang, Q.-Y. Wang, Z. Han, Z.-Y. Wang, X.-Y. Dong, S.-F. Li, S.-Q. Zang, T. C. W. Mak, *J. Am. Chem. Soc.* **2019**, *141*, 14505–14509.

[4] a) H. Liang, B.-J. Liu, B. Tang, S.-C. Zhu, S. Li, X.-Z. Ge, J.-L. Li, J.-R. Zhu, F.-X. Xiao, *ACS Catal.* **2022**, *12*, 4216–4226; b) B. Weng, K.-Q. Lu, Z. Tang, H. M. Chen, Y.-J. Xu, *Nat. Commun.* **2018**, *9*, 1543.

[5] a) Y. Jiang, Y. Yu, X. Zhang, M. Weinert, X. Song, L. Ai, L. Han, H. Fei, *Angew. Chem. Int. Ed.* **2021**, *60*, 17388–17393; *Angew. Chem.* **2021**, *133*, 17528–17533; b) Y. Deng, Z. Zhang, P. Du, X. Ning, Y. Wang, D. Zhang, J. Liu, S. Zhang, X. Lu, *Angew. Chem. Int. Ed.* **2020**, *59*, 6082–6089; *Angew. Chem.* **2020**, *132*, 6138–6145; c) S. Dai, T. Kajiwara, M. Ikeda, I. Romero-Muñiz, G. Patriarche, A. E. Platero-Prats, A. Vimont, M. Daturi, A. Tissot, Q. Xu, C. Serre, *Angew. Chem. Int. Ed.* **2022**, *61*, e202211848; *Angew. Chem.* **2022**, *134*, e202211848.

[6] a) Q. Zhang, S. Gao, J. Yu, *Chem. Rev.* **2023**, *123*, 6039–6106; b) K. L. Kollmannsberger, L. Kronthaler, J. R. Jinschek, R. A. Fischer, *Chem. Soc. Rev.* **2022**, *51*, 9933–9959.

[7] a) Y. Wang, X.-H. Liu, Q. Wang, M. Quick, S. A. Kovalenko, Q.-Y. Chen, N. Koch, N. Pinna, *Angew. Chem. Int. Ed.* **2020**, *59*, 7748–7754; *Angew. Chem.* **2020**, *132*, 7822–7828; b) A. Yao, Y. Du, M. Han, Y. Wang, J. Hu, Q. Zhu, H. Sheng, M. Zhu, *Nano Res.* **2023**, *16*, 1527–1532.

[8] a) H. Furukawa, K. E. Cordova, M. O'Keeffe, O. M. Yaghi, *Science* **2013**, *341*, 1230444; b) H.-C. Zhou, S. Kitagawa, *Chem. Soc. Rev.* **2014**, *43*, 5415–5418; c) J. Liu, T. A. Goetjen, Q.

Wang, J. G. Knapp, M. C. Wasson, Y. Yang, Z. H. Syed, M. Delferro, J. M. Notestein, O. K. Farha, J. T. Hupp, *Chem. Soc. Rev.* **2022**, *51*, 1045–1097; d) X. Zhao, Y. Wang, D.-S. Li, X. Bu, P. Feng, *Adv. Mater.* **2018**, *30*, 1705189; e) A. Ebadi Amooghin, H. Sanaeepur, R. Luque, H. Garcia, B. Chen, *Chem. Soc. Rev.* **2022**, *51*, 7427–7508; f) L. Jiao, H.-L. Jiang, *Chin. J. Catal.* **2023**, *45*, 1–5.

[9] a) Q.-L. Zhu, Q. Xu, *Chem. Soc. Rev.* **2014**, *43*, 5468–5512; b) G. Li, S. Zhao, Y. Zhang, Z. Tang, *Adv. Mater.* **2018**, *30*, 1800702; c) Y.-M. Li, J. Hu, M. Zhu, *Coord. Chem. Rev.* **2023**, *495*, 215364.

[10] a) A. Aijaz, A. Karkamkar, Y. J. Choi, N. Tsumori, E. Rönnebro, T. Autrey, H. Shioyama, Q. Xu, *J. Am. Chem. Soc.* **2012**, *134*, 13926–13929; b) C. Fang, L. Liu, J. Weng, S. Zhang, X. Zhang, Z. Ren, Y. Shen, F. Meng, B. Zheng, S. Li, J. Wu, W. Shi, S. Lee, W. Zhang, F. Huo, *Angew. Chem. Int. Ed.* **2021**, *60*, 976–982; *Angew. Chem.* **2021**, *133*, 989–995; c) X. Li, T. Goh, L. Li, C. Xiao, Z. Guo, X. Zeng, W. Huang, *ACS Catal.* **2016**, *6*, 3461–3468; d) Q. Yang, Q. Xu, H.-L. Jiang, *Chem. Soc. Rev.* **2017**, *46*, 4774–4808; e) M. Mukoyoshi, H. Kitagawa, *Chem. Commun.* **2022**, *58*, 10757–10767; f) Q. Yang, Q. Xu, S.-H. Yu, H.-L. Jiang, *Angew. Chem. Int. Ed.* **2016**, *55*, 3685–3689; *Angew. Chem.* **2016**, *128*, 3749–3753; g) J. Chen, Y. Wang, F. Wang, Y. Li, *Angew. Chem. Int. Ed.* **2023**, *62*, e202218115; *Angew. Chem.* **2023**, *135*, e202218115; h) S. Hu, C. Xie, Y.-P. Xu, X. Chen, M.-L. Gao, H. Wang, W. Yang, Z.-N. Xu, G.-C. Guo, H.-L. Jiang, *Angew. Chem. Int. Ed.* **2023**, *62*, e202311625; *Angew. Chem.* **2023**, *135*, e202311625.

[11] a) Y. Luo, S. Fan, W. Yu, Z. Wu, D. A. Cullen, C. Liang, J. Shi, C. Su, *Adv. Mater.* **2018**, *30*, 1704576; b) Y. Yun, H. Sheng, K. Bao, L. Xu, Y. Zhang, D. Astruc, M. Zhu, *J. Am. Chem. Soc.* **2020**, *142*, 4126–4130; c) H. Wang, X. Liu, W. Yang, G. Mao, Z. Meng, Z. Wu, H.-L. Jiang, *J. Am. Chem. Soc.* **2022**, *144*, 22008–22017; d) Q. You, H. Wang, Y. Zhao, W. Fan, W. Gu, H.-L. Jiang, Z. Wu, *J. Am. Chem. Soc.* **2024**, DOI: 10.1021/jacs.3c13635; e) Y. Zhu, X. Qiu, S. Zhao, J. Guo, X. Zhang, W. Zhao, Y. Shi, Z. Tang, *Nano Res.* **2020**, *13*, 1928–1932.

[12] a) J. Yan, H. Su, H. Yang, S. Malola, S. Lin, H. Häkkinen, N. Zheng, *J. Am. Chem. Soc.* **2015**, *137*, 11880–11883; b) Y. Niihori, Y. Wada, M. Mitsui, *Angew. Chem. Int. Ed.* **2021**, *60*, 2822–2827; *Angew. Chem.* **2021**, *133*, 2858–2863; c) M. S. Bootharaju, C. P. Joshi, M. R. Parida, O. F. Mohammed, O. M. Bakr, *Angew. Chem. Int. Ed.* **2016**, *55*, 922–926; *Angew. Chem.* **2016**, *128*, 934–938.

[13] K. Chu, Y. Luo, D. Wu, Z. Su, J. Shi, J. Z. Zhang, C.-Y. Su, *J. Phys. Chem. Lett.* **2021**, *12*, 8003–8008.

[14] a) M. S. Bootharaju, C. W. Lee, G. Deng, H. Kim, K. Lee, S. Lee, H. Chang, S. Lee, Y.-E. Sung, J. S. Yoo, N. Zheng, T. Hyeon, *Adv. Mater.* **2023**, *35*, 2207765; b) Y. Liu, X. Chai, X. Cai, M. Chen, R. Jin, W. Ding, Y. Zhu, *Angew. Chem. Int. Ed.* **2018**, *57*, 9775–9779; *Angew. Chem.* **2018**, *130*, 9923–9927.

[15] a) S. Yang, W. Hu, X. Zhang, P. He, B. Pattengale, C. Liu, M. Cendejas, I. Hermans, X. Zhang, J. Zhang, J. Huang, *J. Am. Chem. Soc.* **2018**, *140*, 14614–14618; b) K. Sun, M. Liu, J. Pei, D. Li, C. Ding, K. Wu, H.-L. Jiang, *Angew. Chem. Int. Ed.* **2020**, *59*, 22749–22755; *Angew. Chem.* **2020**, *132*, 22937–22943.

[16] Y. Pellegrin, F. Odobel, *C. R. Chim.* **2017**, *20*, 283–295.

[17] a) J. Low, J. Yu, M. Jaroniec, S. Wageh, A. A. Al-Ghamdi, *Adv. Mater.* **2017**, *29*, 1601694; b) J. Zhang, X. Liang, C. Zhang, L. Lin, W. Xing, Z. Yu, G. Zhang, X. Wang, *Angew. Chem. Int. Ed.* **2022**, *61*, e202210849; *Angew. Chem.* **2022**, *134*, e202210849.

[18] a) L. Zhang, R. Long, Y. Zhang, D. Duan, Y. Xiong, Y. Zhang, Y. Bi, *Angew. Chem. Int. Ed.* **2020**, *59*, 6224–6229; *Angew. Chem.* **2020**, *132*, 6283–6288; b) J. Ran, L. Chen, D. Wang, A. Talebian-Kiakalaieh, Y. Jiao, M. Adel Hamza, Y. Qu, L. Jing, K. Davey, S.-Z. Qiao, *Adv. Mater.* **2023**, *35*, 2210164.

Research Articles

Angewandte *Chemie* International Edition

[19] C. Zhang, C. Xie, Y. Gao, X. Tao, C. Ding, F. Fan, H.-L. Jiang, *Angew. Chem. Int. Ed.* **2022**, *61*, e202204108; *Angew. Chem.* **2022**, *134*, e202204108.

[20] a) L. Wang, C. Bie, J. Yu, *Trends Chem.* **2022**, *4*, 973–983; b) M. Zhang, M. Lu, Z.-L. Lang, J. Liu, M. Liu, J.-N. Chang, L.-Y. Li, L.-J. Shang, M. Wang, S.-L. Li, Y.-Q. Lan, *Angew. Chem. Int. Ed.* **2020**, *59*, 6500–6506; *Angew. Chem.* **2020**, *132*, 6562–6568.